

# UC San Diego

## UC San Diego Previously Published Works

### Title

SCALING RELATIONS FOR GALAXIES PRIOR TO REIONIZATION

### Permalink

<https://escholarship.org/uc/item/3t9149c2>

### Journal

The Astrophysical Journal, 795(2)

### ISSN

1538-4357

### Authors

Chen, Pengfei  
Wise, John H  
Norman, Michael L  
[et al.](#)

### Publication Date

2014-10-23

### DOI

10.1088/0004-637X/795/2/144

Peer reviewed

## SCALING RELATIONS FOR GALAXIES PRIOR TO REIONIZATION

PENGFEEI CHEN<sup>1</sup>, JOHN H. WISE<sup>2</sup>, MICHAEL L. NORMAN<sup>1,3</sup>, HAO XU<sup>1</sup>, AND BRIAN W. O’SHEA<sup>4</sup>

<sup>1</sup> CASS, University of California, San Diego, 9500 Gilman Drive, La Jolla, CA 92093, USA; pec008@ucsd.edu, mlnorman@ucsd.edu, hxu@ucsd.edu

<sup>2</sup> Center for Relativistic Astrophysics, School of Physics, Georgia Institute of Technology, 837 State Street, Atlanta, GA 30332, USA; jwise@gatech.edu

<sup>3</sup> SDSC, University of California, San Diego, 9500 Gilman Drive, La Jolla, CA 92093, USA

<sup>4</sup> Lyman Briggs College and Department of Physics and Astronomy, Michigan State University, East Lansing, MI 48824, USA; oshea@msu.edu

Received 2014 August 11; accepted 2014 September 3; published 2014 October 23

### ABSTRACT

The first galaxies in the universe are the building blocks of all observed galaxies. We present scaling relations for galaxies forming at redshifts  $z \geq 15$  when reionization is just beginning. We utilize the “Rarepeak” cosmological radiation hydrodynamics simulation that captures the complete star formation history in over 3300 galaxies, starting with massive Population III stars that form in dark matter halos as small as  $\sim 10^6 M_\odot$ . We make various correlations between the bulk halo quantities, such as virial, gas, and stellar masses and metallicities and their respective accretion rates, quantifying a variety of properties of the first galaxies up to halo masses of  $10^9 M_\odot$ . Galaxy formation is not solely relegated to atomic cooling halos with virial temperatures greater than  $10^4$  K, where we find a dichotomy in galaxy properties between halos above and below this critical mass scale. Halos below the atomic cooling limit have a stellar mass–halo mass relationship  $\log M_* \simeq 3.5 + 1.3 \log(M_{\text{vir}}/10^7 M_\odot)$ . We find a non-monotonic relationship between metallicity and halo mass for the smallest galaxies. Their initial star formation events enrich the interstellar medium and subsequent star formation to a median of  $10^{-2} Z_\odot$  and  $10^{-1.5} Z_\odot$ , respectively, in halos of total mass  $10^7 M_\odot$ , which is then diluted by metal-poor inflows well beyond Population III pre-enrichment levels of  $10^{-3.5} Z_\odot$ . The scaling relations presented here can be employed in models of reionization, galaxy formation, and chemical evolution in order to consider these galaxies forming prior to reionization.

*Key words:* galaxies: formation – galaxies: high-redshift – methods: numerical – radiative transfer

*Online-only material:* color figures

### 1. INTRODUCTION

Low-mass galaxy observations at  $z \gtrsim 6$  naturally have low signal-to-noise ratios with current telescopes because they are distant and intrinsically dim. Nevertheless, recent observational campaigns have provided valuable constraints on the nature of the first galaxies and their central black holes (BHs) and their role during reionization. The Hubble Ultra Deep Field 2009 and 2012 campaigns (Ellis et al. 2013) can probe galaxies with stellar masses as small as  $3 \times 10^8 M_\odot$  at  $z \gtrsim 7$  and as distant as  $z \sim 10$  (McLure et al. 2011; Zheng et al. 2012; Coe et al. 2013; Oesch et al. 2013). From the steep slope of the faint end of the luminosity function (e.g., Bouwens et al. 2011, 2014; McLure et al. 2013), there should be an unseen population of even fainter and more abundant galaxies that will eventually be detected by next-generation telescopes, such as the *James Webb Space Telescope* (launch date 2018; Gardner et al. 2006) and 30 m class ground-based telescopes.<sup>5</sup>

Semi-analytic models and numerical simulations of galaxy formation and evolution (for respective reviews, see Benson 2010; Bromm & Yoshida 2011) are invaluable tools to connect their photometry, spectra, and imaging to the physical properties of their stellar population and dynamics and underlying dark matter (DM) halo. Before making observational predictions, it is necessary to correlate galaxy formation with cosmological structure formation. There are a few methods to make this correlation: halo occupation distribution modeling (e.g., Bullock et al. 2002), conditional luminosity function modeling (e.g.,

Yang et al. 2003), and the abundance matching technique (e.g., Colín et al. 1999; Kravtsov & Klypin 1999; Conroy et al. 2006; Guo et al. 2010). Behroozi et al. (2013, hereafter BWC13) presented a new Markov Chain Monte Carlo method that utilized the observed star formation rates (SFRs) and accordingly the stellar masses of galaxies out to  $z \simeq 8$  to break the degeneracies suffered in other methods, and they were able to constrain the specific SFRs (sSFRs) and cosmic SFRs. Using this method, they also constrained the intrinsic stellar mass–halo mass (SMHM) relation to  $z = 15$  (BWC13; Behroozi & Silk 2014). Their results are consistent with the observed galaxy stellar mass functions, sSFRs, and the cosmic SFR over cosmic time in the halo mass range of  $10^9$ – $10^{15} M_\odot$ .

At the present day, the stellar mass function deviates from the DM halo mass function at both the low-mass and high-mass extremes (e.g., Li & White 2009; Bower et al. 2012). The low-mass deficiency can be attributed to stellar feedback mainly from supernova (SN) explosions and photo-evaporation from the ultraviolet background (e.g., Efstathiou 1992; Bullock et al. 2000; Gnedin 2000; Benson et al. 2002; Okamoto et al. 2008), while a more efficient feedback mechanism, most likely arising from active galactic nuclei (AGNs), is responsible for the high-mass deficiency (e.g., Tabor & Binney 1993; Ciotti & Ostriker 2001; Croton et al. 2006; Dubois et al. 2013; Genel et al. 2014; Schaye et al. 2014).

The SMHM relation for high-redshift dwarfs does not necessarily have the same functional form as the present-day one because of different environmental conditions at high redshift. At the high-mass end, there is some recent observational evidence that the bright end of the galaxy luminosity function does not follow a Schechter function, but possibly a double power law, at  $z \simeq 7$  (Bowler et al. 2014) that could indicate that AGN

<sup>5</sup> European Extremely Large Telescope (39 m, completion date 2024; Gilmozzi & Spyromilio 2007), Giant Magellan Telescope (24.5 m, completion date 2020; Johns et al. 2012), Thirty Meter Telescope (30 m, completion date 2018; Simard 2013).

feedback has not yet quenched star formation in these large galaxies. At the low-mass end, galaxies could be forming in a neutral environment, shielded from any ionizing radiation during reionization, yielding internal stellar feedback as the main suppressant of star formation (Ricotti et al. 2008; Salvadori & Ferrara 2009; Pawlik et al. 2013; Wise et al. 2014).

Furthermore, the first galaxies are directly affected by the radiative, chemical, and mechanical feedback from massive, metal-free (Population III; Pop III) stars (Abel et al. 2002; Bromm et al. 2002; O’Shea & Norman 2007; Turk et al. 2009; Greif et al. 2011a; Hirano et al. 2013; Susa 2013; Susa et al. 2014). Radiative and SN feedback can evacuate the majority of the gas from the host halo (Whalen et al. 2004, 2008; Kitayama et al. 2004; Kitayama & Yoshida 2005; Alvarez et al. 2006; Abel et al. 2007), leaving a gas-poor halo that only recovers by cosmological accretion after tens of Myr (Wise & Abel 2008; Greif et al. 2010; Wise et al. 2012b; Muratov et al. 2013; Jeon et al. 2014b). The Pop III SNe also pre-enrich the gas that ultimately assembles the first galaxies to  $10^{-4}$ – $10^{-3} Z_{\odot}$  (Bromm et al. 2003; Wise & Abel 2008; Karlsson et al. 2008; Greif et al. 2010; Wise et al. 2012b). Prior to cosmological reionization, galaxies can form in DM halos as small as  $10^7 M_{\odot}$ , and these low-mass ( $V_c = \sqrt{GM_{\text{vir}}/R_{\text{vir}}} < 30 \text{ km s}^{-1}$ ) galaxies provide  $\sim 40\%$  of the ionizing photons to reionization, eventually becoming photo-suppressed as reionization ensues (Wise et al. 2014). Afterward, a small fraction (5%–15%) of the first galaxies survive until the present day (Gnedin & Kravtsov 2006), and ultra-faint dwarf galaxies (UFDs) discovered in the Sloan Digital Sky Survey that surround the Milky Way could be the fossils of this subset of the first galaxies. They are very metal-poor (Kirby et al. 2008) and are believed to have had only one or a few early star formation events (Koch 2009; Frebel & Bromm 2012). Unlike the Milky Way halo, which was assembled through multiple merger and accretion events, UFDs likely did not form via extensive hierarchical merging of bound stellar systems (Bovill & Ricotti 2009, 2011a, 2011b; Salvadori & Ferrara 2009; Simpson et al. 2013).

In this paper, we focus on the scaling relations of dwarf galaxies and their relationship to their halos that assemble during the initial stages of reionization. Using cosmological simulations, we extend the relations found by BWC13 to even higher redshifts and smaller galaxies that are the building blocks of all observed galaxies. This work improves the statistics of the first galaxy properties found by Wise et al. (2014) by a factor of 100, whose simulation only captured the formation of 32 galaxies by  $z \simeq 7$ . In addition to unveiling the nature of high-redshift dwarf galaxies, our work can provide valuable constraints on the origin of a subset of dwarf galaxies in the local universe. We have performed a simulation of a survey volume of 135 comoving  $\text{Mpc}^3$  that includes a full primordial chemistry network, radiative cooling from metal species, both Pop III and metal-enriched star formation and their radiative, mechanical and chemical feedback. We first describe our simulation setup in Section 2. Then we present our main results in Section 3. Last we discuss the findings and possible biases in our simulation in Section 4.

## 2. SIMULATION SETUP

We further analyze the ‘‘Rarepeak’’ simulation originally presented in Xu et al. (2013) that focuses on the formation of the first stars and galaxies in a relatively overdense region with  $\langle \delta \rangle \equiv \langle \rho \rangle / (\Omega_M \rho_c) - 1 \simeq 0.65$  at  $z = 15$  in the entire survey volume of 135 comoving  $\text{Mpc}^3$ . Here  $\Omega_M$  is the matter

density in units of the critical density  $\rho_c = 3H_0^2/8\pi G$ . We perform the simulation with the adaptive mesh refinement (AMR) cosmological hydrodynamics code *Enzo* (Bryan et al. 2014). The adaptive ray tracing module *Enzo+Moray* is used for the radiation transport of ionizing photons (Wise & Abel 2011), which is coupled to the hydrodynamics, energy, and chemistry solvers in *Enzo*. We have used this simulation to study the number of Pop III remnants in the first galaxies (Xu et al. 2013), their contribution to the X-ray background (Xu et al. 2014), and the imprint of clustered first galaxies in 21 cm differential brightness temperatures (Ahn et al. 2014). In this paper, we focus on the relationship between the host DM halo and the stellar and gaseous properties of the galaxies. A detailed description of the star formation and feedback models are given in Wise et al. (2012a, 2012b) and Xu et al. (2013), and here we give an overview of the simulation setup and numerical methods.

We generate the initial conditions for the simulation using MUSIC (Hahn & Abel 2011) at  $z = 99$  and use the cosmological parameters from the 7 yr *Wilkinson Microwave Anisotropy Probe*  $\Lambda\text{CDM}+\text{SZ}+\text{LENS}$  best fit (Komatsu et al. 2011):  $\Omega_M = 0.266$ ,  $\Omega_{\Lambda} = 0.734$ ,  $\Omega_b = 0.0449$ ,  $h = 0.71$ ,  $\sigma_8 = 0.81$ , and  $n = 0.963$ , where the variables have the usual definitions. We use a comoving simulation volume of  $(40 \text{ Mpc})^3$  that has a  $512^3$  root grid resolution and three initial nested grids each with mass resolution eight times higher in each nested grid. This corresponds to an effective initial resolution of  $4096^3$  and DM mass resolution of  $2.9 \times 10^4 M_{\odot}$ . The finest nested grid has a comoving volume of  $5.2 \times 7.0 \times 8.3 \text{ Mpc}^3$  ( $302 \text{ Mpc}^3$ ). We allow further refinement in the Lagrangian volume of the finest nested grid up to a maximum AMR level  $l = 12$ , resulting in a maximal spatial resolution of 19 comoving pc. Refinement is triggered by either a baryon or DM overdensity of  $4 \times \Omega_{\{\text{b,DM}\}} \rho_c N^{1/(1+\phi)}$ , respectively. Here  $N = 2$  is the refinement factor, and  $\phi = -0.1$  causes more aggressive refinement at higher densities, i.e., super-Lagrangian behavior. We analyze the simulation at  $z = 15$ , at which point it has 1.3 billion computational cells and consumed over 10 million core-hours on the NICS Kraken and NCSA Blue Waters supercomputers. The Lagrangian region at  $z = 15$  has a comoving volume of  $3.8 \times 5.4 \times 6.6 \text{ Mpc}^3$  ( $135 \text{ Mpc}^3$ ), and we restrict our survey of high-redshift galaxies to this high-resolution region. At this time, the simulation has a large number ( $\sim 1000$ ) of halos with  $M > 10^8 M_{\odot}$ , where new formation of Pop III stars declines rapidly while the formation rate of metal-enriched stars continues to increase. There are three halos with  $M > 10^9 M_{\odot}$  in the refined region at  $z = 15$ .

Both Pop III and metal-enriched stars form in the simulation, which have distinct formation and feedback models, and we distinguish them by the total metallicity of the densest star-forming cell. Pop III stars are formed if  $[Z/H] < -4$ , and metal-enriched stars are formed otherwise. We use the same star formation and feedback models as the ‘‘RP’’ simulation in Wise et al. (2012a) with the exception of the characteristic mass  $M_{\text{char}} = 40 M_{\odot}$  of the Pop III initial mass function (IMF), whereas Wise et al. considered  $100 M_{\odot}$ . To select the Pop III stellar masses, we do not follow the protostellar collapse to high densities and through their protostellar evolution (e.g., Susa et al. 2014), rather we randomly sample from an IMF with the functional form

$$f(\log M) dM = M^{-1.3} \exp \left[ - \left( \frac{M_{\text{char}}}{M} \right)^{1.6} \right] dM \quad (1)$$

that behaves as a power-law IMF at  $M > M_{\text{char}}$  and is exponentially cutoff below that mass (Chabrier 2003). This choice of  $M_{\text{char}}$  is more consistent with the latest results of Pop III formation simulations (e.g., Turk et al. 2009; Greif et al. 2011a; Hirano et al. 2013; Susa 2013; Susa et al. 2014). We treat metal-enriched star formation with the same prescription as Wise & Cen (2009), which is similar to the Pop III prescription but without the minimum  $\text{H}_2$  fraction requirement. This is removed because the metal-enriched gas can efficiently cool even in the presence of a strong UV radiation field (e.g., Safranek-Shrader et al. 2010). To ensure that the stars only form from cold gas, we restrict star formation to gas with temperatures  $T < 1000$  K. Unlike Pop III star particles that represent individual stars, metal-enriched star particles represent a star cluster of some total mass and an assumed normal (i.e., Kroupa) IMF with minimum and maximum stellar masses identical to those inferred in the Milky Way. We set the minimum mass of a star particle to  $m_{\star, \text{min}} = 1000 M_{\odot}$ . If the initial mass does not exceed  $m_{\star, \text{min}}$ , the star particle does not provide any feedback and continues to accrete until it reaches  $m_{\star, \text{min}}$ .

### 3. RESULTS

Our numerical survey focuses on the characteristics and scaling relations of high-redshift galaxies, and we restrict our analysis to halos that are resolved by at least 300 DM particles, corresponding to a mass  $M_{\text{vir}} \simeq 10^7 M_{\odot}$ . There are 3338 such halos in the survey volume at  $z = 15$ . For these halos, we calculate the virial radius  $r_{\text{vir}}$  and mass  $M_{\text{vir}}$ , using an overdensity  $\Delta_{\text{vir}} = 178$  relative to the proper critical density (e.g., Barkana & Loeb 2001). From these halos, we construct halo merger trees. We investigate the growth of the most massive progenitor from each timestep. We also restrict these progenitor halos to contribute at least 50% of their mass to the descendant. Note that the length of a particular merger tree could be less than the total number of snapshots.

We study 64 snapshots from  $z = 18.43$  to  $z = 15.00$ . For all of the halo quantities in each snapshot, including  $M_{\text{vir}}$ ,  $M_{\text{gas}}$ ,  $M_{\star}$  and their accretion rates  $\dot{M}_{\text{vir}}$ ,  $\dot{M}_{\text{gas}}$ ,  $\dot{M}_{\star}$ , we use the time difference between that snapshot and the former snapshot as its weight, since the 64 snapshots are not equally spaced in time because of computational reasons.<sup>6</sup> We explore the correlations between these properties, plus the stellar and gas metallicities, by constructing two-dimensional histograms, in which we include data from all 64 snapshots to increase the sample size. After the  $x$  and  $y$  quantities are binned into histograms with weights, we normalize the histogram values in each  $x$ -bin with sum over  $y$ -axis. Therefore, each histogram value equals the conditional probability in that  $y$ -bin given an  $x$ -value. For each  $x$ -bin we calculate the weighted median, 15.9 and 84.1 percentiles, which are shown as the error bars in all of the figures.

We fit the weighted medians in most of the phase plots with two models: (1) a linear model ( $\log y = A + \alpha \log x$ ) and (2) a smoothed broken power law (SBPL; Ryde 1999). The logarithmic derivative of a SBPL varies smoothly from  $\alpha$  to  $\beta$ :

$$\frac{d \log y}{d \log x} = \xi \tanh \left[ \frac{\log(x/x_b)}{\delta} \right] + \phi, \quad (2)$$

<sup>6</sup> Snapshots exist at equal time intervals, but we utilize the additional outputs that are created at the top-level timestep just before the computing queue time limit is reached.

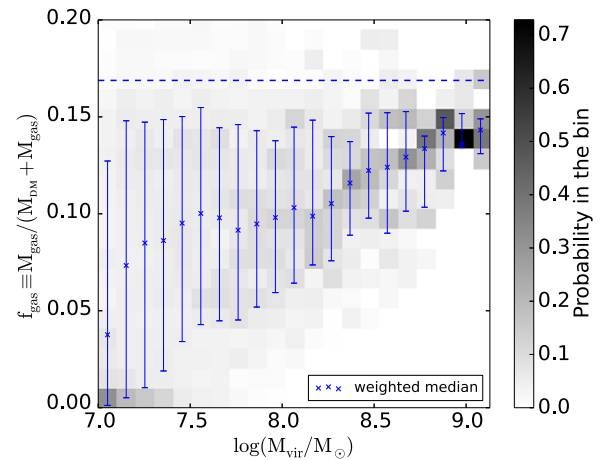


**Figure 1.** Gas fraction of halos as a function of halo mass. As halo mass increases, the effect of stellar feedback becomes less severe, so gas is accreted more efficiently and the scatter of gas fraction decreases. The dashed horizontal line marks the mean baryon fraction  $\Omega_b/\Omega_M$ . The error bars in this figure, along with all of the other figures, depict the 15.9–84.1 percentiles in the distribution. (A color version of this figure is available in the online journal.)

where  $\xi = (\beta - \alpha)/2$ ,  $\phi = (\beta + \alpha)/2$ ,  $x_b$  is the break point.  $\delta$  shows the smoothness of the transition.  $\Delta x = x_b(10^\delta - 1)$  gives the linear width of transition. Integrating Equation (2) gives

$$\log y = A + \phi \log x + (\ln 10)\xi\delta \log \left\{ \cosh \left[ \frac{\log(x/x_b)}{\delta} \right] \right\}. \quad (3)$$

Because the SBPL model is insensitive to  $\delta$ , we fix it to 0.01 in the fits, resulting in four free parameters:  $\{A, \alpha, \beta, x_b\}$ .

All of the fits are performed in log-space, giving a better fit, because these galactic properties vary over several orders of magnitude. The fitting coefficients for all of the relations presented in this work are shown in Table 1. In the last column of the table, we calculate the coefficient of determination  $R^2$  to compare goodness of fit of the two models:

$$R^2 = 1 - \frac{\sum_i (\log y_i - f_i)^2}{\sum_i (\log y_i - \overline{\log y})^2}, \quad (4)$$

where  $\overline{\log y}$  is the average of  $\log y_i$ , and  $f_i$  is the modeled value in log scale. The table shows that the SBPL model always gives a better fit (i.e., a larger  $R^2$ ) than the linear model because it has more parameters.

#### 3.1. Gas Accretion Rates

Figure 1 shows the gas fraction of halos  $f_{\text{gas}} \equiv M_{\text{gas}}/(M_{\text{DM}} + M_{\text{gas}})$  as a function of halo mass  $M_{\text{vir}}$ . The weighted median of gas fraction increases with halo mass, while the scatter of gas fraction decreases. At low masses, halos are susceptible to feedback that is caused either internally through the shock waves generated by H II regions and SNE or externally through photo-evaporation by a strong ionizing UV flux originating from nearby galaxies. The large scatter represents the different levels of feedback experienced by such halos, for example, varying Pop III stellar masses and endpoints (i.e., an SN or direct BH formation) or being embedded in a large-scale neutral or ionized region. At  $z = 15$ , halos with mass  $M = 3 \times 10^8 M_{\odot}$  have circular velocities  $V_c \simeq 30 \text{ km s}^{-1}$ , holding the gas tenuously in its gravitational grasp. Around and above this mass scale, the gas fractions nearly recover to the cosmic mean gas fraction

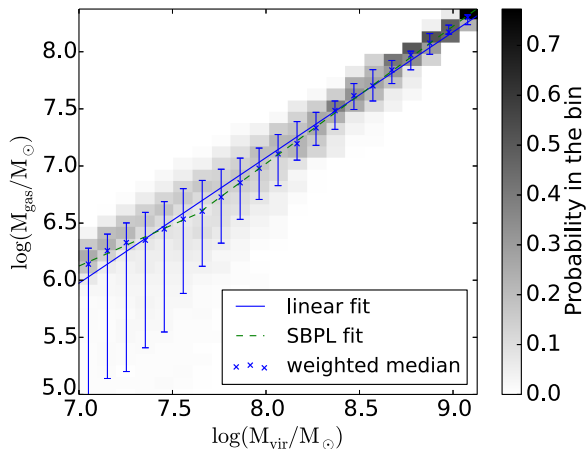
**Table 1**  
Coefficients for the Scaling Relation Fits to the Weighted Medians

Figure	Relation	Model	$A$	$\alpha$	$\beta$	$x_b$	$R^2$
2	$M_{\text{gas}}$ vs. $M_{\text{vir}}$	Linear	$-1.72 \pm 0.37$	$1.10 \pm 0.05$			0.99
		SBPL	$-0.76 \pm 0.33$	$0.72 \pm 0.09$	$1.20 \pm 0.02$	$(4.32 \pm 0.78) \times 10^7$	1.00
3(a)	$\dot{M}_{\text{gas}}/\dot{M}_{\text{vir}}$ vs. $M_{\text{vir}}$	Linear	$-1.95 \pm 0.33$	$0.13 \pm 0.04$			0.71
3(b)	$\dot{M}_{\star}$ vs. $M_{\text{vir}}$	Linear	$-13.15 \pm 1.21$	$1.41 \pm 0.15$			0.95
		SBPL	$-13.16 \pm 0.77$	$0.78 \pm 0.15$	$1.97 \pm 0.13$	$(1.05 \pm 0.24) \times 10^8$	1.00
3(c)	$\dot{M}_{\star}/\dot{M}_{\text{vir}}$ vs. $M_{\text{vir}}$	Linear	$-5.63 \pm 1.17$	$0.43 \pm 0.14$			0.67
		SBPL	$-5.29 \pm 1.21$	$-0.19 \pm 0.24$	$0.88 \pm 0.17$	$(9.14 \pm 3.72) \times 10^7$	0.92
5	$M_{\star}$ vs. $M_{\text{vir}}$	Linear	$-9.88 \pm 0.84$	$1.88 \pm 0.10$			0.99
		SBPL	$-9.05 \pm 0.67$	$1.31 \pm 0.16$	$2.18 \pm 0.08$	$(6.97 \pm 1.81) \times 10^7$	1.00
6(a)	$\dot{M}_{\star}$ vs. $\dot{M}_{\text{gas}}$	Linear	$-1.61 \pm 0.15$	$0.50 \pm 0.08$			0.77
		SBPL	$-1.91 \pm 0.23$	$0.28 \pm 0.17$	$0.77 \pm 0.21$	$0.11 \pm 0.21$	0.82
6(b)	$\dot{M}_{\star}$ vs. $\dot{M}_{\text{vir}}$	Linear	$-2.06 \pm 0.12$	$0.34 \pm 0.08$			0.60
		SBPL	$-2.61 \pm 0.28$	$-0.19 \pm 0.28$	$0.55 \pm 0.12$	$0.14 \pm 0.18$	0.75
7(a)	$[Z/H]_{\text{gas}}$ vs. $M_{\text{vir}}$	SBPL	$-5.79 \pm 1.92$	$-0.27 \pm 0.36$	$1.16 \pm 0.31$	$(1.02 \pm 0.48) \times 10^8$	0.86
7(b)	$[Z/H]_{\star}$ vs. $M_{\text{vir}}$	SBPL	$-4.29 \pm 1.75$	$-0.82 \pm 0.33$	$1.32 \pm 0.29$	$(1.08 \pm 0.31) \times 10^8$	0.88
8(a)	$[Z/H]_{\text{gas}}$ vs. $M_{\text{gas}}$	SBPL	$-5.10 \pm 1.45$	$-0.29 \pm 0.04$	$1.07 \pm 0.37$	$(1.01 \pm 0.57) \times 10^7$	0.90
8(b)	$[Z/H]_{\star}$ vs. $M_{\text{gas}}$	SBPL	$-8.74 \pm 5.11$	$-0.22 \pm 0.06$	$1.99 \pm 1.28$	$(4.30 \pm 2.52) \times 10^7$	0.76
9(a)	$[Z/H]_{\text{gas}}$ vs. $M_{\star}$	SBPL	$-4.27 \pm 0.64$	$-0.11 \pm 0.11$	$0.84 \pm 0.18$	$(4.17 \pm 2.75) \times 10^5$	0.92
9(b)	$[Z/H]_{\star}$ vs. $M_{\star}$	SBPL	$-4.54 \pm 1.51$	$-0.21 \pm 0.17$	$1.01 \pm 0.44$	$(7.29 \pm 7.40) \times 10^5$	0.70
10	$[Z/H]_{\star}$ vs. $[Z/H]_{\text{gas}}$	SBPL	$-0.37 \pm 0.30$	$0.93 \pm 0.22$	$-0.14 \pm 0.32$	$0.10 \pm 0.12$	0.91
		SBPL <sup>a</sup>	$-0.31 \pm 0.30$	$1.03 \pm 0.10$	$-0.32 \pm 0.90$	$0.11 \pm 0.10$	0.96 <sup>b</sup>

**Notes.** All the fits are performed in log-scale for the linear fit, which is  $\log y = A + \alpha \log x$ , and the smoothed broken power law (SBPL, Equation (3)), where  $\alpha$  and  $\beta$  are the slopes below and above the break point  $x_b$ . The  $R^2$  measure defined in Equation (4) indicates the goodness of the fit. Errors shown have a confidence of 95%.

<sup>a</sup> Instead of having the same weight for all the weighted medians, this SBPL fit uses the sum of the time weights in each  $x$ -bin as the weight of the weighted median of data in that  $x$ -bin.

<sup>b</sup> The definition of  $R^2$  for fitting data with weights requires changing all the sums in Equation (4) into weighted sums.



**Figure 2.** Mass of gas in halos as a function of halo mass. With a slope of 1.1, mass of gas increases almost linearly with halo mass. Fitting results are shown in Table 1.

(A color version of this figure is available in the online journal.)

$\Omega_b/\Omega_M$  as baryons can withstand the effects of stellar feedback and photo-evaporation. We show mass of gas as a function of halo mass in Figure 2, where mass of gas increases almost linearly with halo mass ( $M_{\text{gas}} \propto M_{\text{vir}}^{1.1}$ ), while the scatter of  $M_{\text{gas}}$  decreases with  $M_{\text{vir}}$ . The slope is greater than unity because there is a transition from a gas-poor to gas-rich accretion mode in this mass range. The SBPL model is physically motivated by the nature of gas accretion changing in atomic cooling halos, and

it provides a better fit with a break at  $(4.32 \pm 0.78) \times 10^7 M_{\odot}$ , approximately the halo mass with a  $T_{\text{vir}} = 10^4$  K at  $z = 15$ . Below and above the break, the gas mass–halo mass relation has a slope of  $0.72 \pm 0.09$  and  $1.20 \pm 0.02$ , respectively. At higher masses, we expect the slope to flatten to less than unity so that it never exceeds  $M_{\text{vir}}$ .

Figure 3(a) shows  $\dot{M}_{\text{gas}}/\dot{M}_{\text{vir}}$  as a function of  $M_{\text{vir}}$ . Although  $\dot{M}_{\text{gas}}/\dot{M}_{\text{vir}}$  is almost constant ( $\dot{M}_{\text{gas}} \sim 0.1 \dot{M}_{\text{vir}}$ ), a small positive slope of the fitting line means more massive halos are attracting gas more efficiently. However, in general, halos do not always accrete gas, where low-mass halos are the most susceptible to strong outflows and gas loss from radiative and SN feedback because of their shallow potential wells. This can be inferred from the observation that  $\sim 13\%$  of the data points have  $\dot{M}_{\text{gas}} < 0$ , which are included when calculating weighted medians and curve fittings but not shown in the histogram. Most (90%) of these halos with a net gas outflow have  $M_{\text{vir}} < 10^{7.5} M_{\odot}$ . The large scatter in the low-mass halos are mainly due to variations in  $\dot{M}_{\text{gas}}$ . Lower mass halos are more affected by their star formation history. Specifically, the gas accretion rate depends on the feedback it has experienced in the past. If the halo hosted a less massive ( $\sim 10$ – $30 M_{\odot}$ ) Pop III star, then less gas would be expelled by the radiative and SN feedback. However, if the halo hosted a more massive star ( $> 60 M_{\odot}$ ), then most of the gas would have been expelled due to its higher luminosity. Massive halos form from the merger of many smaller halos, which serves to average out the differences seen in these halos and results in less scatter in the gas accretion rates. Another effect that could

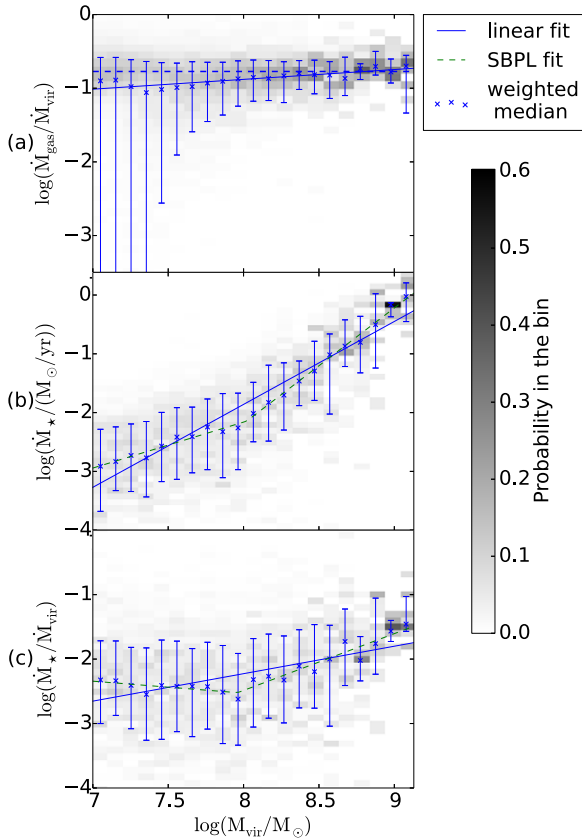


**Figure 3.** (a) Gas accretion rate over halo mass accretion rate as a function of halo mass. Negative gas accretion rate is included when calculating weighted medians. The weighted medians of this ratio are almost constant. Large scatters for low-mass halos are due to stellar feedback. The lower ends of the first four error bars are  $-2 \times 10^{-5}$ ,  $-7 \times 10^{-5}$ ,  $-5 \times 10^{-3}$ , and  $-9 \times 10^{-5}$ . The dashed horizontal line marks the mean baryon fraction  $\Omega_b/\Omega_M$ . (b) Star formation rate as a function of halo mass. A clear transition shows up at  $M_{\text{vir}} \sim 10^8 M_\odot$ , after which the metal-enriched star formation becomes more efficient. (c) Star formation rate over halo mass accretion rate as a function of halo mass, showing an upturn in star formation above  $\sim 10^8 M_\odot$ .

(A color version of this figure is available in the online journal.)

cause the larger scatter is environment, that is, whether it is near a larger galaxy and is partially photo-evaporated by an external radiation field.

### 3.2. Star Formation Efficiency

The star formation efficiency  $f_*$ , i.e., the fraction of gas in a halo that eventually forms stars, can be influenced by stellar feedback, internal dynamics, and the size of the gas reservoir available for star formation, among other factors. It is an inherently multi-scale problem, where some fraction of the accreted or in situ gas cools and condenses into dense molecular clouds, and then some fraction of that molecular gas proceeds to form stars. Here we will focus on the connection between star formation and the host halo and large-scale accretion rates.

#### 3.2.1. Dependence on Halo Mass

We show the stellar fraction of halos  $f_* \equiv M_*/M_{\text{gas}}$  as a function of halo mass  $M_{\text{vir}}$  in Figure 4. Most of the low-mass halos have  $f_*$  values of around a few percent, because soon after a trace amount of stars form,  $\text{H}_2$  is photo-dissociated throughout the halo by the radiative, specifically local Lyman–Werner, and SN feedback, first sterilizing the gas and then disrupting any possible star formation sites. This delays the formation of

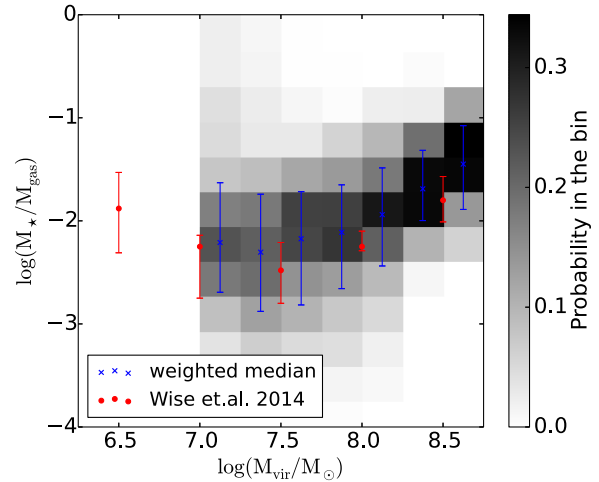


**Figure 4.** Stellar fraction as a function of halo mass. Each cross point is the weighted median of the data points in that  $x$ -bin. For halos with  $M_{\text{vir}} < 10^{7.5} M_\odot$ , we restrict the median to galaxies with  $f_* < 0.25$  to focus on the star-forming halos. These results are consistent with the higher resolution simulation of Wise et al. (2014), represented by the red circles.

(A color version of this figure is available in the online journal.)

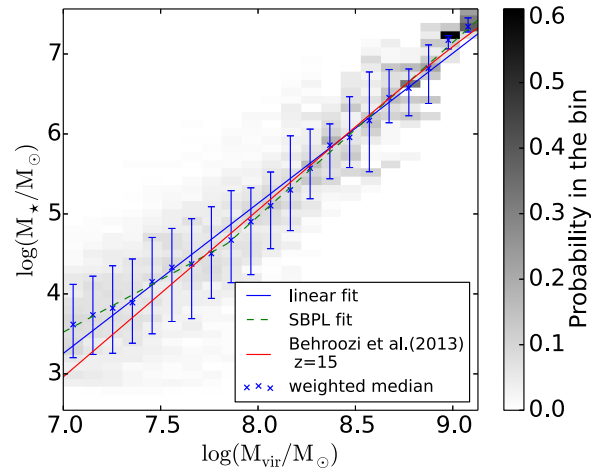


**Figure 5.** Stellar mass–halo mass (SMHM) relation compared with the relation from Behroozi et al. (2013).

(A color version of this figure is available in the online journal.)

subsequent stars until halos reach  $T_{\text{vir}} \sim 10^4$  K (Haïman et al. 2000; Ciardi et al. 2000). There are 5% of total halos with a high stellar fractions  $f_* > 0.2$ , and nearly all of these halos (98%) have  $M_{\text{vir}}$  less than  $10^{7.5} M_\odot$ . These high fractions occur when stellar feedback expels a large fraction of gas, leaving behind a gas-poor halo, thus increasing  $f_*$ . This behavior was previously shown in the gas accretion rates, and the gas reservoir only recovers later through cosmological gas accretion above  $T_{\text{vir}} = 10^4$  K. In these larger atomic cooling halos, stellar feedback has less of an effect. First, the total SN energies are less than the binding energy of the halo, and, second, the  $\text{H II}$  regions are mostly contained within the halo, reducing gas blowout from ionization fronts. In Figure 4, the points show the weighted medians of all the  $f_*$  at  $M_{\text{vir}} > 10^{7.5} M_\odot$ , and we restrict the median to only include galaxies with  $f_* < 0.25$  below that mass scale to focus on objects that are actively forming stars in relatively gas-rich halos.

The SMHM relation is shown in Figure 5. Since there is no observational data at such high redshifts, we compare our results with the SMHM relation of BWC13 that considers observations

up to  $z \simeq 8$ . Since their fitting formula explicitly depends on redshift and halo mass, we compare their fit at  $z = 15$  to our simulated SMHM relation, even though this extrapolates beyond the bounds of their original work. We choose the redshift where the simulation ends because roughly 60% of our data points are in the range  $z = 15$ – $16$ . The slope  $\alpha = 1.88 \pm 0.10$  of the linear fit is larger than unity (see Table 1) because this halo mass range probes a regime where a transition from inefficient to efficient star formation mode occurs. As with the gas accretion relations, the SBPL models this transition better with the slope increasing from  $\alpha = 1.31 \pm 0.16$  to  $\beta = 2.18 \pm 0.08$  at a break point of  $\sim 7 \times 10^7 M_\odot$ . The slope  $\beta$  is closer to the model of BWC13, and we expect the slope to flatten at higher masses as star formation becomes self-regulated after this initial burst during the transition to an atomic cooling halo. The model of BWC13 also showed that at  $z \leq 6$  the slope becomes flatter at halo masses  $M \gtrsim 10^{12} M_\odot$  at which point galaxies grow primarily through accreting bound stellar systems instead of forming new stars (e.g., Conroy & Wechsler 2009). The massive end of the stellar mass function appears to be approximately in place since  $z \sim 1$  (e.g., Wake et al. 2006; Brown et al. 2007; Cool et al. 2008).

We show  $\dot{M}_*$  as a function of  $M_{\text{vir}}$  in Figure 3(b). While the average  $\dot{M}_*$  always increases with  $M_{\text{vir}}$ , there is a clear change of slope at  $\sim 10^8 M_\odot$ . A similar change could be seen from Figure 3(c), which shows  $\dot{M}_*/\dot{M}_{\text{vir}}$  as a function of  $M_{\text{vir}}$ . There are several possible contributing factors to this transition. First, halos larger than  $\sim 10^8 M_\odot$  are not sensitive to the stellar feedback so they can attract gas more efficiently. Second, their virial temperature  $T_{\text{vir}} \gtrsim 10^4$  K, at which point hydrogen atomic line cooling becomes efficient. Lastly, the most massive halos have hosted numerous SN explosions and have been metal enriched and established a metallicity floor at lower halo masses. We explore the correlations between metallicity and halo properties shortly in Section 3.3.

### 3.2.2. Dependence on Mass Accretion Rates

We show  $\dot{M}_*$  as a function of  $\dot{M}_{\text{gas}}$  in Figure 6(a), which measures the fraction of accreted gas that forms stars if we consider this process to be instantaneous. Overall,  $\dot{M}_*$  increases as approximately  $\dot{M}_{\text{gas}}^{0.5}$ , but at  $10^{-2.5} M_\odot \text{ yr}^{-1}$  and  $10^{0.8} M_\odot \text{ yr}^{-1}$ , the increase in stellar mass is greater than the overall trend but still consistent with the fit. We have few DM halos with high ( $\gtrsim 10 M_\odot \text{ yr}^{-1}$ ) or low ( $\lesssim 10^{-3} M_\odot \text{ yr}^{-1}$ ) gas accretion rates, which corresponds to the high-probability points. Figure 6(b) shows  $\dot{M}_*$  as a function of  $\dot{M}_{\text{vir}}$ . Above a mass accretion rate  $\dot{M}_{\text{vir}} > 0.1 M_\odot \text{ yr}^{-1}$ , the slope of this relation is nearly equal to the  $\dot{M}_* - \dot{M}_{\text{gas}}$  relation because the gas and mass accretion rates have little dependence on halo mass above  $\sim 10^8 M_\odot$  (see Figure 3(a)). However below  $0.1 M_\odot \text{ yr}^{-1}$ , the SFR has little dependence on the mass accretion rates. This regime occurs when the halo experiences little growth from both mergers and smooth accretion, so that any increase in stellar mass must originate from gas that is already present in the halo. In these small halos, star formation is regulated to a low SFR of  $\sim 10^{-3} M_\odot \text{ yr}^{-1}$  without any fresh supply of accreted mass to instigate further star formation.

### 3.3. Metallicity

The gas-phase and stellar metallicities of galaxies are intimately related to their SFRs and IMFs. The first galaxies are both enriched by Pop III and metal-enriched stars during their

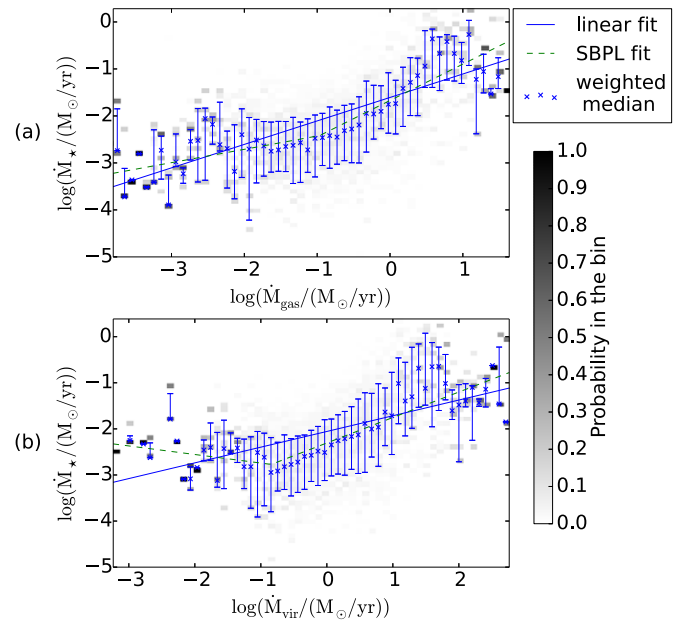


**Figure 6.** (a) Star formation rate as a function of gas mass accretion rate. (b) Star formation rate as a function of halo mass accretion rate.

(A color version of this figure is available in the online journal.)

assembly. Here we investigate the correlations between these metallicities and the halo mass and growth. In the following analysis, we calculate the mass-averaged gas-phase ( $[Z/H]_{\text{gas}}$ ) and stellar ( $[Z/H]_*$ ) metallicities within the virial radius of each halo with  $M_{\text{vir}} > 10^7 M_\odot$ . The metallicities include contributions from SNe originating from both Pop III and metal-enriched stars, and we only include metal-enriched stars in the stellar metallicity statistics.

#### 3.3.1. Dependence on Virial and Gas Mass

We show both the mean gas metallicity  $[Z/H]_{\text{gas}}$  and stellar metallicity  $[Z/H]_*$  as a function of halo mass in Figure 7. The large scatter in  $[Z/H]_{\text{gas}}$  at low masses show the dependence on the Pop III SN that occurs in the halo progenitors. Some of the halos with  $M_{\text{vir}} < 10^{7.5} M_\odot$  have nearly primordial metallicities because they have not hosted an SN due to the randomness of the Pop III IMF. In other words, they have either formed a Pop III star with a BH endpoint or no star formation has occurred in this halo. The highest metallicities might be coming from the Pop III SNe exploding in more massive halos, and the ejecta is being trapped mostly inside of the minihalos (Whalen et al. 2008; Ritter et al. 2012). There is a metallicity floor of  $[Z/H]_{\text{gas}} \sim -3.5$  for halos more massive than  $10^{7.5} M_\odot$ , most of which have been enriched by SN explosions. Similarly, damped Ly $\alpha$  absorbers (DLAs) have a metallicity floor of  $\sim 10^{-2.8} Z_\odot$  out to  $z \sim 5$  (e.g., Wolfe et al. 2005; Penprase et al. 2010; Rafelski et al. 2012), and the metallicity distribution functions of Milky Way halo stars and local dwarf galaxies precipitously drop below a similar metallicity (e.g., Battaglia et al. 2006; Kirby et al. 2011; McConnachie 2012; An et al. 2013), suggesting that both extremely metal-poor DLAs and stars have been enriched primarily by SNe from Pop III stars (e.g., Bromm et al. 2003; Wise & Abel 2008; Karlsson et al. 2008; Greif et al. 2010; Wise et al. 2012b).

We find that the metallicity floor is slightly smaller than  $[Z/H]_{\text{gas}} \sim -3$  in Wise et al. (2012b) because we use a lower  $M_{\text{char}}$  in Equation (1) that favors hypernovae instead of

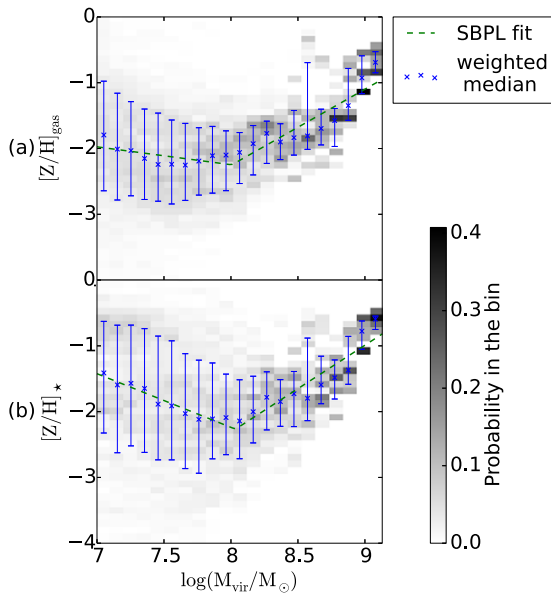


**Figure 7.** Mass-averaged metallicity as a function of halo mass. A metallicity floor of  $[Z/H]_{\text{gas}} \sim -3.5$  is shown for halos more massive than  $10^{7.5} M_{\odot}$  with the median metallicity one to two orders of magnitude higher. After an initial starburst, which is often triggered by SN blastwaves (biasing the stellar metallicity median at the lowest masses), the accretion of pristine and metal-poor gas results in the drop of the weighted median of gas metallicity with increasing halo masses up to  $10^8 M_{\odot}$ . In larger halos, the metallicity increases because metal-enriched star formation becomes efficient, and the metal-rich SN ejecta enrich the galaxy.

(A color version of this figure is available in the online journal.)

pair-instability SN. For instance, the metal ejecta from a  $40 M_{\odot}$  hypernova is  $8.6 M_{\odot}$  (Nomoto et al. 2006), compared to  $85 M_{\odot}$  of metals produced by a  $180 M_{\odot}$  pair-instability SN (Heger & Woosley 2002), while the hypernova explosion energies are lower by a factor of a few. Below a halo mass of  $10^8 M_{\odot}$ , the gas-phase metallicity slowly decreases with halo mass ( $[Z/H]_{\text{gas}} \propto M_{\text{vir}}^{-0.27}$ ) because the gas is initially enriched by Pop III SNe and then as metal-free and metal-poor gas accretes into the halo, this initial enrichment is diluted. The effects of dilution is also apparent in Figure 8 where the gas-phase metallicity is generally lower than the stellar metallicity. In larger halos, metal-enriched star formation becomes more efficient, enriching itself, which is apparent in the weighted median of  $[Z/H]_{\text{gas}}$  increasing as  $M_{\text{vir}}^{1.16}$ . Because metal-enriched stars form from this enriched gas,  $[Z/H]_{*}$  approximately follows the distribution of  $[Z/H]_{\text{gas}}$  in these atomic cooling halos.

However, in the lower mass halos, the dilution is more apparent in the stellar metallicity than the gas-phase metallicity because the star formation can occur in triggered events as blastwaves overtake nearby dense clouds inside the halo, leading to high metallicities, which is reflected in the steeper negative slope in the stellar metallicity relation. Afterward, the halo experiences a period without star formation. Once the diluted ejecta recollects in the potential well of the halo, star formation recommences at a lower metallicity, reflected by the negative slope in the stellar metallicity–halo mass relation. Figure 8 better illustrates this sequence of enrichment, blowout, and re-accretion in dependence of the gas-phase and stellar metallicities on the gas mass of the halo. Here it is clear that the gas-poor halos have a higher metallicity than their gas-rich counterparts. They have most of their gas blown out by SNe, leaving behind a medium that is more enriched, whereas the more gas-rich halos have been replenished through further gas accretion.

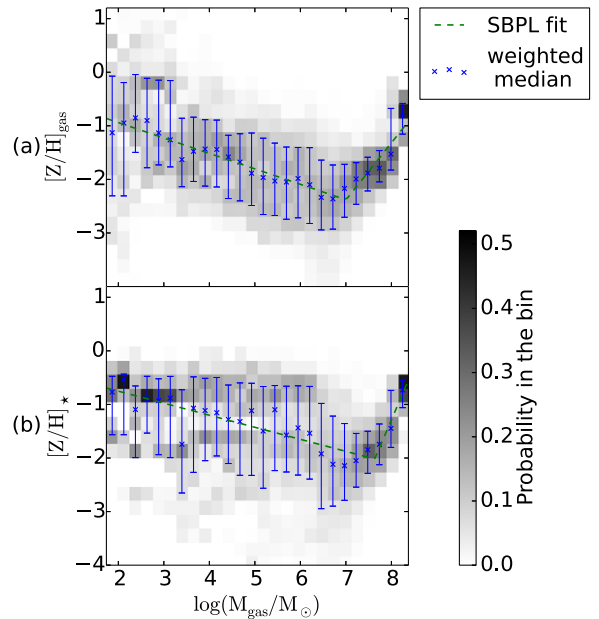


**Figure 8.** Mass-averaged gas-phase (top) and stellar (bottom) metallicity as a function of gas mass.

(A color version of this figure is available in the online journal.)

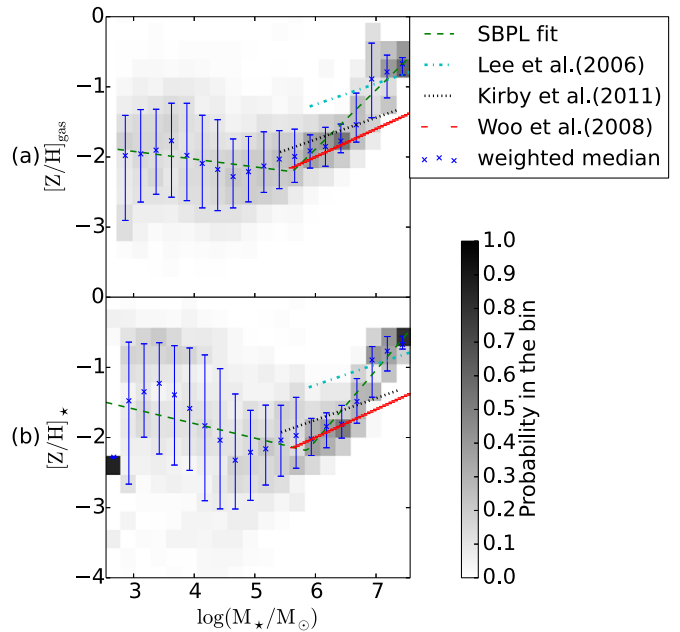


**Figure 9.** Mass-averaged gas-phase (top) and stellar (bottom) metallicities as a function of stellar mass compared with three observational relations, restricted to their original ranges.

(A color version of this figure is available in the online journal.)

### 3.3.2. Dependence on Stellar Mass

In Figure 9, we show the metallicity–stellar mass relations and compare them with a few observational results. At a stellar mass  $M_{*} \lesssim 10^5 M_{\odot}$ , the gas-phase and stellar metallicities decrease as a function of stellar mass for the reasons described previously. Above this mass, we can compare our simulated stellar populations to the metallicity–stellar mass relations in local dwarf galaxies. Although this is not a one-to-one comparison, it gives some constraints on the validity of our simulations because a fraction of these galaxies will survive until

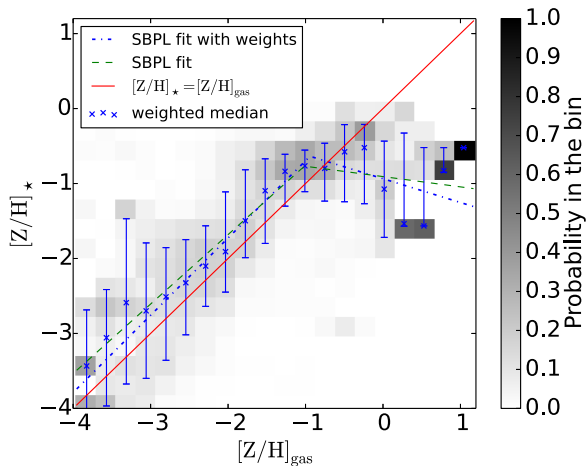


**Figure 10.** Mass-averaged stellar metallicity versus gas metallicity. The dash-dotted line shows the SBPL fit to the weighted halo data, and the dashed line shows the SBPL fit to the weighted medians. The solid line is the equivalence line for comparison. Most of the halos with low gas metallicity are self-enriched by SN explosions. The median of the stellar metallicity is generally higher than the gas metallicity, occurring because the SNe ejecta is constantly being diluted through a combination of metal-rich outflows and metal-poor inflows.

(A color version of this figure is available in the online journal.)

the present day without significant star formation (e.g., Gnedin & Kravtsov 2006; Bovill & Ricotti 2011a; Simpson et al. 2013). Furthermore, once the galaxy starts to enrich itself from in situ star formation, the stellar metallicity will only increase from these values at  $z = 15$ . However, these comparisons should be viewed as qualitative comparisons because local dwarf galaxies undergo some amount of tidal harassment as it orbits around the Milky Way, lowering their stellar content. In addition, their metallicity distribution functions will, in principle, be altered during this process because the more metal-poor stars are less centrally concentrated than the “metal-rich” component in local dwarfs (Tolstoy et al. 2004; Battaglia et al. 2006).

Kirby et al. (2011) used measurements of iron absorption lines in the central regions of eight dwarf satellite galaxies of the Milky Way, whose stellar masses range from  $10^{5.4}$  to  $10^{7.4} M_{\odot}$ . Woo et al. (2008) analyzed oxygen abundance data of  $\sim 40$  dwarf galaxies with  $M_{\star}$  ranging from  $10^{5.6}$  to  $10^{9.6} M_{\odot}$ . Both of their results fit well with our  $\sim 10^{5.5}$ – $10^7 M_{\odot}$  galaxies, but above this mass range, the metallicities of the simulated galaxies increase by nearly an order of magnitude. However, the metallicities in the most massive galaxies in our simulation better match with the results of Lee et al. (2006), who analyzed interstellar medium oxygen abundance measurements of 25 dwarf galaxies with stellar mass  $M_{\star}$  ranging from  $10^{5.9}$  to  $10^{9.3} M_{\odot}$ . This stellar mass range corresponds to halo masses  $M \gtrsim 10^9 M_{\odot}$  (see Figure 5), where we simulate three halos at this scale. Because these galaxies are at the center of large-scale potential well and are experiencing high-mass accretion rates, they may have higher SFRs and thus enrichment rates than present-day dwarf galaxies, whereas the lower mass galaxies are possibly regulated by photo-evaporation from a strong UV radiation field that originates from the central galaxies, keeping their SFRs and metallicities low.

### 3.3.3. Correlation between Stellar and Gas-phase Metallicities

Figure 10 compares the correlation between stellar and gas metallicities. An equivalence line  $[Z/H]_{\star} = [Z/H]_{\text{gas}}$  is plotted for comparison. For most halos with  $[Z/H]_{\text{gas}} < -1$ , their

stellar metallicities are larger than the gas-phase metallicities because the gas is constantly being diluted by a combination of SN-driven metal-rich outflows and an inflow of metal-poor gas. However, in most of the more metal-enriched halos ( $[Z/H]_{\text{gas}} > -1$ ), the stellar metallicities are smaller than the gas-phase ones with 14% of the data shown in Figure 10 in this regime, and 85% of which are in halos of virial mass  $M_{\text{vir}} < 10^8 M_{\odot}$ . This corresponds to the scenario where SN-driven outflow rates are higher than the inflow rates of metal-poor gas.

## 4. DISCUSSION AND CONCLUSIONS

In this paper, we present several scaling relations for galaxies that form in an overdense region at  $z \gtrsim 15$ , including correlations between bulk halo properties (virial, gas, and stellar masses), their growth (accretion rates and SFRs), and chemical enrichment (gas-phase and stellar metallicities). We derived these relationships from a zoom-in cosmological radiation hydrodynamics simulation that considers both metal-free and metal-enriched star formation and feedback. We model the effects of radiative feedback using the radiation transport module *Enzo+Moray*. The high-resolution region contains over 3300 star-forming halos with the three most massive halos having  $M \sim 10^9 M_{\odot}$ .

This simulation represents the largest simulated sample of first galaxies to date and confirms that the first galaxies are not restricted to atomic cooling halos with virial temperatures  $T_{\text{vir}} \gtrsim 10^4$  K, where we have shown that the SMHM extends down to  $10^7 M_{\odot}$  halos, which are adequately sampled by 300 DM particles in our simulation. The scaling relations presented here demonstrate that there is a clear distinction between halos below and above this critical mass scale corresponding to  $T_{\text{vir}} = 10^4$  K. Confirming the results of Salvadori & Ferrara (2009) and Wise et al. (2014), halos with  $T_{\text{vir}} \lesssim 10^4$  K cool through transitions in  $\text{H}_2$  and metals, forming stars at a slower rate at  $\dot{M}_{\star} \propto M_{\text{vir}}^{\alpha}$  with  $\alpha = 0.78 \pm 0.15$ , only to form stars more efficiently at  $\alpha = 1.97 \pm 0.13$  when hydrogen line cooling becomes dominant in our sample of simulated first galaxies.

The correlations presented in this paper, summarized in Table 1, can be utilized in a number of studies that have not considered star formation in such small halos prior to reionization. Some examples are (1) semi-analytic models of galaxy formation (e.g., Benson 2010; Gómez et al. 2014), (2) reionization calculations either using semi-analytic, semi-numerical, or  $N$ -body simulations (e.g., Zahn et al. 2011; Alvarez et al. 2012), (3) subgrid models of unresolved star formation (Trenti & Stiavelli 2007), and (4) chemical evolution models (e.g., Salvadori et al. 2007; Tumlinson 2010; Crosby et al. 2013). For instance, including halos that host low levels of star formation into a reionization calculation would produce a more extended reionization history, better matching constraints provided by the cosmic microwave background (Zahn et al. 2012; Planck Collaboration et al. 2013) and the  $z \sim 6$  Gunn–Peterson troughs (Fan et al. 2006). Furthermore, our metallicity relationships include the pre-enrichment from Pop III stars, so they provide a robust set of initial conditions for the first galaxies, evolving to present-day galaxies.

Although our simulation includes most of the relevant physical processes during the formation of the first galaxies, there are a few shortcomings in our work that we will address in later studies. First, the DM resolution only captures the star formation in halos with masses  $M \gtrsim 3 \times 10^6 M_{\odot}$ ; however, in an overdense region, we expect the intergalactic UV radiation

field to be high, with Lyman–Werner radiation suppressing Pop III star formation in halos smaller than our resolution limit (Machacek et al. 2001; Wise & Abel 2007; O’Shea & Norman 2008). Furthermore, supersonic relative velocities between DM and baryons that originate during recombination can also suppress star formation in these minihalos (Tsaliakhovich & Hirata 2010; Tsaliakhovich et al. 2011; Greif et al. 2011b; Stacy et al. 2011; Naoz et al. 2012). We also do not consider the local X-ray radiative feedback from Pop III BH remnants that could play a role in further regulating star formation within the galaxy (Alvarez et al. 2009; Xu et al. 2013, 2014; Jeon et al. 2014a). Concerning our analysis methods, we include all of the data in the redshift range  $z = 18.4\text{--}15$  as being time independent. We did this to increase the sample size under the assumption that the SMHM relation is weakly dependent on redshift, and furthermore, this redshift range corresponds to only 70 Myr. We can also justify this simplification by inspecting the SMHM relation found in BWC13 that shows the largest difference in stellar mass at a fixed halo mass is less than 1 dex over all cosmic time.

This work represents an important step forward in quantifying a variety of properties of the first galaxies (see Table 1), using a sample of over 3300 star-forming halos at  $z \geq 15$ . The highlights of our findings are as follows.

1. Halos with virial temperatures  $T_{\text{vir}} \lesssim 10^4$  K can cool through  $\text{H}_2$  and fine-structure metal lines, prompting a burst of star formation and creating a stellar population with  $\log M_\star \simeq 3.5 + 1.3 \log (M_{\text{vir}}/10^7 M_\odot)$ . In atomic cooling halos, this slope increases to  $\sim 2.2$ , indicating more efficient star formation. This SMHM relation is consistent with the results of Salvadori & Ferrara (2009), BWC13, and Wise et al. (2014).
2. After an initial star formation event that expels most of the gas from the halo, the median of the gas fraction never fully recovers to the cosmic mean  $\Omega_b/\Omega_M$  in the halo mass range presented here. The median at  $10^8 M_\odot$  is approximately 10% and increases to 15% as the halos grow another order of magnitude.
3. During this initial star formation event, SN blastwaves further enrich the galaxy well beyond Pop III pre-enrichment levels to a median of  $[Z/H] \sim -1.5$  in halos with total and stellar masses of  $10^7 M_\odot$  and  $10^{3.5} M_\odot$ , respectively. The metallicities decrease with halo mass as pristine and metal-poor gas accumulates through mergers and smooth accretion. After the halo can cool through atomic line cooling, the galaxy begins to enrich itself continuously through sustained and efficient star formation.

Our simulation captures and quantifies the formation of the first galaxies. However, we warn that our results are sampled from an overdense region that is not necessarily representative of the cosmic mean. We showed in Xu et al. (2013) that the halo mass function at  $z = 15$  is about five times that of the cosmic mean and is similar to the abundances found at  $z = 10$ . Our results should not change significantly in regions of different large-scale overdensities, although these biased halos could experience higher mass accretion rates than ones situated in more typical or underdense regions of the universe. To address this issue, we are following up this study with two more zoom-in simulations of a region of mean matter density, and also a void region, all within the same  $(40 \text{ Mpc})^3$  volume, and we will present their results at a later date.

This research was supported by National Science Foundation (NSF) grant AST-1109243 to M.L.N. J.H.W. acknowledges support from NSF grants AST-1211626 and AST-1333360. B.W.O. was supported in part by the MSU Institute for Cyber-Enabled Research and the NSF through grant PHY-0941373. The simulation was performed on the Kraken supercomputer operated for the Extreme Science and Engineering Discovery Environment (XSEDE) by the National Institute for Computational Science, ORNL with XRAC allocation MCA-TG98020N, and on the Blue Waters operated by the National Center for Supercomputing Applications (NCSA) with PRAC allocation support by the NSF (award number OCI-0832662). Data analysis was performed on the Gordon supercomputer operated for XSEDE by the San Diego Supercomputer Center and on the Blue Waters supercomputer. This research is part of the Blue Waters sustained-petascale computing project, which is supported by the NSF (award number ACI-1238993) and the state of Illinois. Blue Waters is a joint effort of the University of Illinois at Urbana-Champaign and the NCSA. This research has made use of NASA’s Astrophysics Data System Bibliographic Services. Computations and associated analysis described in this work were performed using the publicly available *Enzo* code (<http://enzo-project.org>) and the *yt* toolkit (<http://yt-project.org>; Turk et al. 2011), which are the products of collaborative efforts of many independent scientists from numerous institutions around the world. Their commitment to open science has helped make this work possible.

## REFERENCES

- Abel, T., Bryan, G. L., & Norman, M. L. 2002, *Sci*, 295, 93  
 Abel, T., Wise, J. H., & Bryan, G. L. 2007, *ApJL*, 659, L87  
 Ahn, K., Xu, H., Norman, M. L., Alvarez, M. A., & Wise, J. H. 2014, arXiv:1405.2085  
 Alvarez, M. A., Bromm, V., & Shapiro, P. R. 2006, *ApJ*, 639, 621  
 Alvarez, M. A., Finlator, K., & Trenti, M. 2012, *ApJL*, 759, L38  
 Alvarez, M. A., Wise, J. H., & Abel, T. 2009, *ApJL*, 701, L133  
 An, D., Beers, T. C., Johnson, J. A., et al. 2013, *ApJ*, 763, 65  
 Barkana, R., & Loeb, A. 2001, *PhR*, 349, 125  
 Battaglia, G., Tolstoy, E., Helmi, A., et al. 2006, *A&A*, 459, 423  
 Behroozi, P. S., & Silk, J. 2014, arXiv:1404.5299  
 Behroozi, P. S., Wechsler, R. H., & Conroy, C. 2013, *ApJ*, 770, 57 (BWC13)  
 Benson, A. J. 2010, *PhR*, 495, 33  
 Benson, A. J., Frenk, C. S., Lacey, C. G., Baugh, C. M., & Cole, S. 2002, *MNRAS*, 333, 177  
 Bouwens, R. J., Illingworth, G. D., Oesch, P. A., et al. 2011, *ApJ*, 737, 90  
 Bouwens, R. J., Illingworth, G. D., Oesch, P. A., et al. 2014, arXiv:1403.4295  
 Bovill, M. S., & Ricotti, M. 2009, *ApJ*, 693, 1859  
 Bovill, M. S., & Ricotti, M. 2011a, *ApJ*, 741, 17  
 Bovill, M. S., & Ricotti, M. 2011b, *ApJ*, 741, 18  
 Bower, R. G., Benson, A. J., & Crain, R. A. 2012, *MNRAS*, 422, 2816  
 Bowler, R. A. A., Dunlop, J. S., McLure, R. J., et al. 2014, *MNRAS*, 440, 2810  
 Bromm, V., Coppi, P. S., & Larson, R. B. 2002, *ApJ*, 564, 23  
 Bromm, V., & Yoshida, N. 2011, *ARA&A*, 49, 373  
 Bromm, V., Yoshida, N., & Hernquist, L. 2003, *ApJL*, 596, L135  
 Brown, M. J. I., Dey, A., Jannuzi, B. T., et al. 2007, *ApJ*, 654, 858  
 Bryan, G. L., Norman, M. L., O’Shea, B. W., et al. 2014, *ApJS*, 211, 19  
 Bullock, J. S., Kravtsov, A. V., & Weinberg, D. H. 2000, *ApJ*, 539, 517  
 Bullock, J. S., Wechsler, R. H., & Somerville, R. S. 2002, *MNRAS*, 329, 246  
 Chabrier, G. 2003, *PASP*, 115, 763  
 Ciardi, B., Ferrara, A., Governato, F., & Jenkins, A. 2000, *MNRAS*, 314, 611  
 Ciotti, L., & Ostriker, J. P. 2001, *ApJ*, 551, 131  
 Coe, D., Zitrin, A., Carrasco, M., et al. 2013, *ApJ*, 762, 32  
 Colin, P., Klypin, A. A., Kravtsov, A. V., & Khokhlov, A. M. 1999, *ApJ*, 523, 32  
 Conroy, C., & Wechsler, R. H. 2009, *ApJ*, 696, 620  
 Conroy, C., Wechsler, R. H., & Kravtsov, A. V. 2006, *ApJ*, 647, 201  
 Cool, R. J., Eisenstein, D. J., Fan, X., et al. 2008, *ApJ*, 682, 919  
 Crosby, B. D., O’Shea, B. W., Peruta, C., Beers, T. C., & Tumlinson, J. 2013, arXiv:1312.0606  
 Croton, D. J., Springel, V., White, S. D. M., et al. 2006, *MNRAS*, 365, 11

- Dubois, Y., Gavazzi, R., Peirani, S., & Silk, J. 2013, *MNRAS*, **433**, 3297
- Efstathiou, G. 1992, *MNRAS*, **256**, 43
- Ellis, R. S., McLure, R. J., Dunlop, J. S., et al. 2013, *ApJL*, **763**, L7
- Fan, X., Carilli, C. L., & Keating, B. 2006, *ARA&A*, **44**, 415
- Frebel, A., & Bromm, V. 2012, *ApJ*, **759**, 115
- Gardner, J. P., Mather, J. C., Clampin, M., et al. 2006, *SSRv*, **123**, 485
- Genel, S., Vogelsberger, M., Springel, V., et al. 2014, arXiv:1405.3749
- Gilmozzi, R., & Spyromilio, J. 2007, *Msngr*, **127**, 11
- Gnedin, N. Y. 2000, *ApJ*, **542**, 535
- Gnedin, N. Y., & Kravtsov, A. V. 2006, *ApJ*, **645**, 1054
- Gómez, F. A., Coleman-Smith, C. E., O'Shea, B. W., Tumlinson, J., & Wolpert, R. L. 2014, *ApJ*, **787**, 20
- Greif, T. H., Glover, S. C. O., Bromm, V., & Klessen, R. S. 2010, *ApJ*, **716**, 510
- Greif, T. H., Springel, V., White, S. D. M., et al. 2011a, *ApJ*, **737**, 75
- Greif, T. H., White, S. D. M., Klessen, R. S., & Springel, V. 2011b, *ApJ*, **736**, 147
- Guo, Q., White, S., Li, C., & Boylan-Kolchin, M. 2010, *MNRAS*, **404**, 1111
- Hahn, O., & Abel, T. 2011, *MNRAS*, **415**, 2101
- Haiman, Z., Abel, T., & Rees, M. J. 2000, *ApJ*, **534**, 11
- Heger, A., & Woosley, S. E. 2002, *ApJ*, **567**, 532
- Hirano, S., Hosokawa, T., Yoshida, N., et al. 2013, *ApJ*, **781**, 60
- Jeon, M., Pawlik, A. H., Bromm, V., & Milosavljević, M. 2014a, *MNRAS*, **440**, 3778
- Jeon, M., Pawlik, A. H., Bromm, V., & Milosavljević, M. 2014b, arXiv:1407.0034
- Johns, M., McCarthy, P., Raybould, K., et al. 2012, *Proc. SPIE*, **8444**, 84441
- Karlsson, T., Johnson, J. L., & Bromm, V. 2008, *ApJ*, **679**, 6
- Kirby, E. N., Lanfranchi, G. A., Simon, J. D., Cohen, J. G., & Guhathakurta, P. 2011, *ApJ*, **727**, 78
- Kirby, E. N., Simon, J. D., Geha, M., Guhathakurta, P., & Frebel, A. 2008, *ApJL*, **685**, L43
- Kitayama, T., & Yoshida, N. 2005, *ApJ*, **630**, 675
- Kitayama, T., Yoshida, N., Susa, H., & Umemura, M. 2004, *ApJ*, **613**, 631
- Koch, A. 2009, *AN*, **330**, 675
- Komatsu, E., Smith, K. M., Dunkley, J., et al. 2011, *ApJS*, **192**, 18
- Kravtsov, A. V., & Klypin, A. A. 1999, *ApJ*, **520**, 437
- Lee, H., Skillman, E. D., Cannon, J. M., et al. 2006, *ApJ*, **647**, 970
- Li, C., & White, S. D. M. 2009, *MNRAS*, **398**, 2177
- Machacek, M. E., Bryan, G. L., & Abel, T. 2001, *ApJ*, **548**, 509
- McConnachie, A. W. 2012, *AJ*, **144**, 4
- McLure, R. J., Dunlop, J. S., Bowler, R. A. A., et al. 2013, *MNRAS*, **432**, 2696
- McLure, R. J., Dunlop, J. S., de Ravel, L., et al. 2011, *MNRAS*, **418**, 2074
- Muratov, A. L., Gnedin, O. Y., Gnedin, N. Y., & Zemp, M. 2013, *ApJ*, **772**, 106
- Naoz, S., Yoshida, N., & Gnedin, N. Y. 2012, *ApJ*, **747**, 128
- Nomoto, K., Tominaga, N., Umeda, H., Kobayashi, C., & Maeda, K. 2006, *NuPhA*, **777**, 424
- Oesch, P. A., Bouwens, R. J., Illingworth, G. D., et al. 2013, *ApJ*, **773**, 75
- Okamoto, T., Gao, L., & Theuns, T. 2008, *MNRAS*, **390**, 920
- O'Shea, B. W., & Norman, M. L. 2007, *ApJ*, **654**, 66
- O'Shea, B. W., & Norman, M. L. 2008, *ApJ*, **673**, 14
- Pawlik, A. H., Milosavljević, M., & Bromm, V. 2013, *ApJ*, **767**, 59
- Penprase, B. E., Prochaska, J. X., Sargent, W. L. W., Toro-Martinez, I., & Beeler, D. J. 2010, *ApJ*, **721**, 1
- Planck Collaboration, Ade, P. A. R., Aghanim, N., et al. 2013, arXiv:1303.5076
- Rafelski, M., Wolfe, A. M., Prochaska, J. X., Neeleman, M., & Mendez, A. J. 2012, *ApJ*, **755**, 89
- Ricotti, M., Gnedin, N. Y., & Shull, J. M. 2008, *ApJ*, **685**, 21
- Ritter, J. S., Safrank-Shrader, C., Gnat, O., Milosavljević, M., & Bromm, V. 2012, *ApJ*, **761**, 56
- Ryde, F. 1999, *ApL&C*, **39**, 281
- Safrank-Shrader, C., Bromm, V., & Milosavljević, M. 2010, *ApJ*, **723**, 1568
- Salvadori, S., & Ferrara, A. 2009, *MNRAS*, **395**, L6
- Salvadori, S., Schneider, R., & Ferrara, A. 2007, *MNRAS*, **381**, 647
- Schaye, J., Crain, R. A., Bower, R. G., et al. 2014, arXiv:1407.7040
- Simard, L. 2013, *JApA*, **34**, 97
- Simpson, C. M., Bryan, G. L., Johnston, K. V., et al. 2013, *MNRAS*, **432**, 1989
- Stacy, A., Bromm, V., & Loeb, A. 2011, *ApJL*, **730**, L1
- Susa, H. 2013, *ApJ*, **773**, 185
- Susa, H., Hasegawa, K., & Tominaga, N. 2014, *ApJ*, **792**, 32
- Tabor, G., & Binney, J. 1993, *MNRAS*, **263**, 323
- Tolstoy, E., Irwin, M. J., Helmi, A., et al. 2004, *ApJL*, **617**, L119
- Trenti, M., & Stiavelli, M. 2007, *ApJ*, **667**, 38
- Tseliakhovich, D., Barkana, R., & Hirata, C. M. 2011, *MNRAS*, **418**, 906
- Tseliakhovich, D., & Hirata, C. 2010, *PhRvD*, **82**, 083520
- Tumlinson, J. 2010, *ApJ*, **708**, 1398
- Turk, M. J., Abel, T., & O'Shea, B. 2009, *Sci*, **325**, 601
- Turk, M. J., Smith, B. D., Oishi, J. S., et al. 2011, *ApJS*, **192**, 9
- Wake, D. A., Nichol, R. C., Eisenstein, D. J., et al. 2006, *MNRAS*, **372**, 537
- Whalen, D., Abel, T., & Norman, M. L. 2004, *ApJ*, **610**, 14
- Whalen, D., van Veelen, B., O'Shea, B. W., & Norman, M. L. 2008, *ApJ*, **682**, 49
- Wise, J. H., & Abel, T. 2007, *ApJ*, **671**, 1559
- Wise, J. H., & Abel, T. 2008, *ApJ*, **685**, 40
- Wise, J. H., & Abel, T. 2011, *MNRAS*, **414**, 3458
- Wise, J. H., Abel, T., Turk, M. J., Norman, M. L., & Smith, B. D. 2012a, *MNRAS*, **427**, 311
- Wise, J. H., & Cen, R. 2009, *ApJ*, **693**, 984
- Wise, J. H., Demchenko, V. G., Halicek, M. T., et al. 2014, *MNRAS*, **442**, 2560
- Wise, J. H., Turk, M. J., Norman, M. L., & Abel, T. 2012b, *ApJ*, **745**, 50
- Wolfe, A. M., Gawiser, E., & Prochaska, J. X. 2005, *ARA&A*, **43**, 861
- Woo, J., Courteau, S., & Dekel, A. 2008, *MNRAS*, **390**, 1453
- Xu, H., Ahn, K., Wise, J. H., Norman, M. L., & O'Shea, B. W. 2014, *ApJ*, **791**, 110
- Xu, H., Wise, J. H., & Norman, M. L. 2013, *ApJ*, **773**, 83
- Yang, X., Mo, H. J., & van den Bosch, F. C. 2003, *MNRAS*, **339**, 1057
- Zahn, O., Mesinger, A., McQuinn, M., et al. 2011, *MNRAS*, **414**, 727
- Zahn, O., Reichardt, C. L., Shaw, L., et al. 2012, *ApJ*, **756**, 65
- Zheng, W., Postman, M., Zitrin, A., et al. 2012, *Natur*, **489**, 406